remote sensing

Article

MCSPF-Net: A Precipitation Forecasting Method Using Multi-Channel Cloud Observations of FY-4A Satellite by 3D Convolution Neural Network

Yuhang Jiang [1], Feng Gao [1,2], Shaoqing Zhang [1,3], Wei Cheng [4], Chang Liu [1,*] and Shudong Wang [5]

1 College of Intelligent Systems Science and Engineering, Harbin Engineering University, Harbin 150001, China; jiangyh97@hrbeu.edu.cn (Y.J.); gaofeng19@hrbeu.edu.cn (F.G.); szhang@ouc.edu.cn (S.Z.)
2 Qingdao Innovation and Development Center, Harbin Engineering University, Qingdao 266400, China
3 Key Laboratory of Physical Oceanography, MOE, Institute for Advanced Ocean Study, Frontiers Science Center for Deep Ocean Multispheres and Earth System (DOMES), The College of Ocean and Atmosphere, Ocean University of China, Qingdao 266100, China
4 Beijing Institute of Applied Meteorology, Beijing 100029, China; chengw@mail.iap.ac.cn
5 Public Meteorological Service Center, China Meterological Administration, Beijing 100081, China; wangsd@cma.gov.cn
* Correspondence: liuchang407@hrbeu.edu.cn

Abstract: Accurate precipitation forecasting plays an important role in disaster prevention and mitigation. Currently, precipitation forecasting mainly depends on numerical weather prediction and radar observation. However, ground-based radar observation has limited coverage and is easily influenced by the environment, resulting in the limited coverage of precipitation forecasts. The infrared observations of geosynchronous earth orbit (GEO) satellites have been widely used in precipitation estimation due to their extensive coverage, continuous monitoring, and independence from environmental influences. In this study, we propose a multi-channel satellite precipitation forecasting network (MCSPF-Net) based on 3D convolutional neural networks. The network uses real-time multi-channel satellite observations as input to forecast precipitation for the future 4 h (30-min intervals), utilizing the observation characteristics of GEO satellites for wide coverage precipitation forecasting. The experimental results showed that the precipitation forecasting results of MCSPF-Net have a high correlation with the Global Precipitation Measurement product. When evaluated using rain gauges, the forecasting results of MCSPF-Net exhibited higher critical success index (0.25 vs. 0.21) and correlation coefficients (0.33 vs. 0.23) and a lower mean square error (0.36 vs. 0.93) compared to the numerical weather prediction model. Therefore, the multi-channel satellite observation-driven MCSPF-Net proves to be an effective approach for predicting near future precipitation.

Keywords: precipitation forecasting; neural network; satellite; AGRI

check for updates

Citation: Jiang, Y.; Gao, F.; Zhang, S.; Cheng, W.; Liu, C.; Wang, S. MCSPF-Net: A Precipitation Forecasting Method Using Multi-Channel Cloud Observations of FY-4A Satellite by 3D Convolution Neural Network. *Remote Sens.* **2023**, *15*, 4536. https://doi.org/10.3390/rs15184536

Academic Editor: Seon Ki Park

Received: 14 August 2023
Revised: 12 September 2023
Accepted: 13 September 2023
Published: 15 September 2023

1. Introduction

In recent years, climate change has led to frequent disastrous weather, resulting in a large number of casualties and economic losses and inconvenience to people's production and life [1]. Precipitation is one of the causes of disastrous weather, and accurate precipitation forecasting has become an urgent need [2–4]. In addition, among various weather phenomena, the occurrence of precipitation has a greater impact on people's production and life, and accurate short-term precipitation forecasts will bring great convenience to people [5,6]. Therefore, short-term precipitation forecasting has received widespread attention. However, the current ability to forecast heavy rainfall and other types of heavy precipitation is still limited, especially the center of precipitation, precipitation intensity and duration of the forecast accuracy is not high. These reasons make accurate precipitation forecasting still challenging [7,8]. Therefore, it is of great significance to improve the accuracy of short-term precipitation forecasts.

The current short-term precipitation forecasting technology mainly depends on numerical weather prediction (NWP) and radar observation. NWP has an irreplaceable role in medium-term and long-term weather forecasting. However, the NWP method is limited by the accuracy of the initial field and a large amount of computation, which has some limitations in short-term precipitation forecasting [9]. The future radar echo variations are forecasted by obtaining historical radar observation data, and the precipitation is quantitatively forecasted by the Z-R relationship [10,11]. In recent years, deep learning technology has developed rapidly. In the field of meteorology, more and more work applying deep learning techniques has shown better forecasting results. Shi et al. proposed the ConvLSTM model [12], which is superior to the traditional optical flow method in the short-term forecasting of precipitation, and it provides a feasible scheme for short-term precipitation forecasting based on deep learning. On this basis, Wang et al. proposed the Pred-RNN model to enhance the learning ability of the model to the temporal and spatial variation characteristics [13] while enhancing the performance of deep learning in precipitation forecasting. Sonderby et al. proposed the Met-Net model to achieve precipitation forecasting by integrating GOES-R satellite observation and multi-radar/multi-sensor (MRMS) system observations [14]. These methods very well resolve the problem of short-term precipitation forecasting. However, the deployment of radar has problems such as a limited number of stations, limited observation range, and sensibility to electromagnetic and topographic interference. The existence of these problems makes the service coverage and stability of short-term precipitation forecasts based on radar observations challenging. With the rapid progress of meteorological satellite technology, the limitations of the observation range of traditional observation methods at the current stage have been alleviated to a certain extent. The extensive coverage, continuous monitoring, and independence from environmental influences capabilities of satellites have filled a large number of observation gaps and provided strong support for researchers to understand the changes in atmospheric systems [15].

At present, there are two main methods for precipitation estimation using satellites: IR sensors on a geosynchronous earth orbit meteorological satellite and passive microwave sensors on a polar orbit satellite. The infrared (IR) sensor can provide high spatial and temporal resolution observation images and has the ability to continuously detect the same region [16]. The estimation of precipitation by the IR sensor depends on a certain relationship between the lower cloud top brightness temperature and the precipitation rate [17]. By analyzing the brightness temperature of the satellite observations, the precipitation estimation product of the current region is obtained [18,19]. However, this method has the risk of failure and is not stable enough. The passive microwave sensor is mounted on a polar orbiting satellite, where microwaves have the ability to penetrate clouds and are scattered by water and ice crystals in the clouds as a way to measure clouds in three dimensions. This measurement method is more direct than the IR sensor and has a solid physical foundation in precipitation estimation [20,21]. However, polar orbit satellites have the problems of narrow observation range and low sampling frequency, which does not allow continuous observation of the same area. In order to solve this problem, the Global Precipitation Measurement Integrated Multi-satellitE Retrievals for GPM (GPM-IMERG) products use a multi-satellite joint inversion method to achieve precipitation estimation. Although it makes up for the low sampling frequency, product production takes a long time, which greatly affects the real-time performance of satellite observations. According to the characteristics of GEO satellites, IR sensors can better track and detect precipitation processes in precipitation monitoring and independently realize grid-based precipitation estimation. In addition, the GEO satellite also fills the missing observation of polar orbiting satellites and assists in constructing gridded precipitation estimation products [22].

With the rapid development of deep learning technology in recent years, a variety of satellite precipitation estimation methods based on deep learning methods have been proposed [23–25]. Hsu et al. proposed Precipitation Estimation from Remotely Sensed Information using Artificial Neural Networks (PERSIANN) [26], which use geosynchronous orbit satellites as input to realize precipitation estimation. Hong et al. proposed an estimation of Precipitation Estimation from Remotely Sensed Information using Artificial Neural Networks Cloud Classification System (PERSIANN-CCS) to extract the texture features of clouds and cluster cloud patches into well-organized subgroups [27], and then, they established the relationship between the cloud top temperature and precipitation rate and assigned the precipitation rate of each group of clouds. Wang et al. proposed a GEO satellite infrared precipitation estimation method IPEC-FY based on a convolutional neural network [28,29]. The pre-training scheme was used to obtain the gridded precipitation estimation results and achieve the best estimation performance. These methods use the combination of multi-channel observation data of the GEO satellite to realize the precipitation estimation task of the GEO satellite, which provides a feasible scheme for the infrared multi-channel precipitation estimation task of the GEO satellite. However, the ability of high spatial and temporal resolution and large-scale observation of GEO satellites still have great potential for applications [30]. With this observation ability, the use of geosynchronous orbit satellites for short-term precipitation forecasting will greatly improve the coverage of short-term forecasting. The minute-level precipitation forecasting covers more areas with missing observations.

This study proposes a multi-channel satellite short-term precipitation forecasting method based on deep learning. This method will be used as a supplement to the short-term precipitation forecasting method to make up for the limited coverage of short-term precipitation forecasting based on radar observation at the current stage. In this study, a multi-channel satellite precipitation forecasting network (MCSPF-Net) based on three-dimensional convolution is designed according to the characteristics of the multi-channel observations of the FY-4A satellite. Using the encoding ability of three-dimensional convolution to time and space features, the precipitation forecasting of multi-channel satellite observation images is realized. In addition, a multi-scale feature extraction module is added to the network. The design of this module is inspired by the ideas of inception and depthwise separable convolution [31,32]. The model has the ability to extract features at different scales, and it relies on depthwise separable convolution to reduce the parameters of the model. The model inputs multi-channel historical satellite observation time-series data, and the short-term precipitation forecast ability based on multi-channel satellite observation can be obtained through training the network. Compared with the GPM-IMERG product and the rain gauge equipped with the ground observation station, the model can accurately predict the precipitation in the next 4 h. It is proved that MCSPF-Net can accurately forecast precipitation based on GEO satellite IR observation images. Furthermore, this study represents an exploratory effort to investigate the potential application of GEO satellite infrared observations in precipitation forecasting. Encouragingly, this study has achieved promising forecasting performance, demonstrating the viability and effectiveness of utilizing such a network for accurate precipitation forecasting. And such a method also has the ability to be extended to other regions, which is an important supplement to the current precipitation forecasting methods.

This paper is organized as follows. Section 2 presents the data we used and the method of constructing the dataset; in Section 3, the construction of our MCSPF-Net and the method of the training model is presented; Section 4 contains the band combination scheme performance comparison and model performance evaluation using multiple data sources; in Section 5, the performance and significance of the MCSPF-net network are discussed; in Section 6, the conclusion of this paper is presented.

2. Data

This section will introduce the data used in the study, including the FY-4A satellite infrared observation images, GPM-IMERG precipitation products, and rain gauge data from ground observation stations. In this section, the use and construction methods of various datasets will be introduced in detail.

2.1. FY-4A

The Fengyun-4A satellite is a new generation of geosynchronous earth orbit meteorological satellites in China, which is equipped with an advanced scanning radiation imager (AGRI) with a wide range of scanning capabilities [33]. AGRI has 14 different bands, including visible light channel, near infrared channel, water vapor channel, and infrared channel. The spatial resolutions of different bands are different with spatial resolutions of 500 m,1000 m, 2000 m, and 4000 m, respectively. The AGRI bands observation information of the FY-4A satellite is shown in Table 1. AGRI can continuously scan the Chinese region at a minimum interval of 15 min, continuously monitor the change of cloud top, and make timely warnings of dangerous weather [34,35]. Compared with the previous generation of satellites, the spatial resolution and scanning time interval have been greatly improved [36]. In this study, the water vapor band and the infrared band of the FY-4A satellite AGRI L1-level full-disk 4000 m resolution observation data will be used for multi-channel satellite precipitation forecasting tasks. The FY-4A products are available online: http://satellite.nsmc.org.cn/PortalSite/Data/Satellite.aspx (accessed on 9 September 2023). The bands visualization results required in the experiment are shown in Figure 1.

Table 1. The AGRI bands observation information of the FY-4A satellite [1].

Spectral Coverage	Central Wavelength	Spectral Bandwidth	Spatial Resolution	Main Applications
Visible	0.47 µm	0.45–0.49 µm	1 km	Aerosol
	0.65 µm	0.55–0.75 µm	0.5–1 km	Fog, cloud
	0.825 µm	0.75–0.90 µm	1 km	Vegetation
Short-wave infrared	1.375 µm	1.36–1.39 µm	2 km	Cirrus
	1.61 µm	1.58–1.64 µm	2 km	Cloud, snow
	2.25 µm	2.1–2.35 µm	2–4 km	Cirrus, aerosol
Mid-wave infrared	3.75 µm	3.5–4.0 µm	2 km	Fire
	3.75 µm	3.5–4.0 µm	2 km	Land surface
Water vapor	6.25 µm	5.8–6.7 µm	4 km	Upper-level water vapor
	7.1 µm	6.9–7.3 µm	4 km	Mid-level water vapor
Long-wave infrared	8.5 µm	8.0–9.0 µm	4 km	Volcanic, ash, cloud top, phase
	10.7 µm	10.3–11.3 µm	4 km	Sea surface temperature, Land surface temperature
	12.0 µm	11.5–12.5 µm	4 km	Clouds, low-level water vapor
	13.5 µm	13.2–13.8 µm	4 km	Clouds, air temperature

[1] Available online: http://www.nsmc.org.cn/nsmc/en/instrument/AGRI.html (accessed on 12 September 2023).

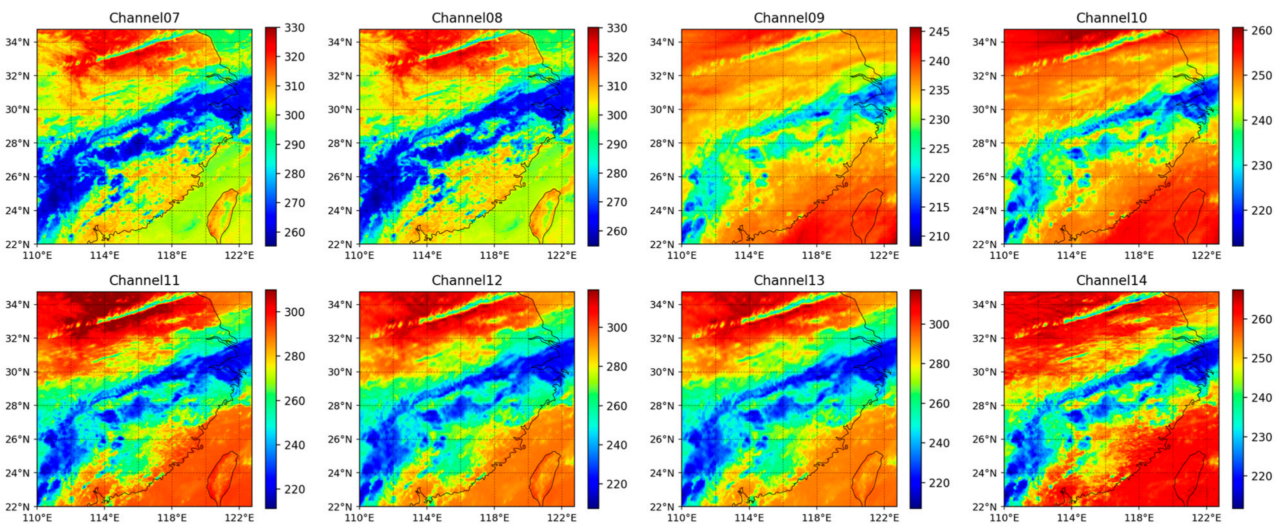

Figure 1. FY-4A satellite AGRI infrared bands visual image (example time 3 June 2020).

2.2. Evaluation Data

The precipitation dataset of this study uses the GPM-IMERG product. As the successor of the TRMM program, the GPM program has greatly improved in accuracy and spatial and temporal resolution [37]. The L3-level product GPM-IMERG uses a variety of satellites and sensors to jointly invert precipitation, including GPM, TRMM, NOAA, METOP and other satellites and the observation instruments they carry. These satellite data are important sources for GPM-IMERG products to obtain global precipitation information. By combining multiple satellite data, more accurate and detailed global precipitation information can be obtained [38]. After the adjustment of various algorithms, the gridded precipitation product with half-hour time resolution and $0.1^\circ \times 0.1^\circ$ spatial resolution is finally obtained. Its Final Run version is also corrected by ground stations [39]. This also makes the inversion data of the Final Run version more accurate and widely recognized [40]. However, the GPM-IMERG Final Run version data have a long delay, and the data produced are about 3.5 months later than the satellite observation data [41]. The GPM-IMERG products are available online: https://gpm.nasa.gov/data/directory (accessed on 9 September 2023). Based on this feature, the GPM-IMERG data are also used as the precipitation label data during the training of the model in this study.

This study used the precipitation results measured by rain gauges equipped with ground observation stations in China as evaluation data. As a direct observation method, the rain gauge equipped with ground observation stations has higher accuracy than data from other sources, but its spatial representation is low and is often used in the evaluation process of precipitation products. Therefore, this paper uses the automatic station rain gauge observation data with 1 h time resolution, and the data include 1 h cumulative precipitation.

Concurrently, we have selected the Weather Research and Forecasting (WRF) model for a comparative analysis within the context of the MCSPF-Net's precipitation forecasting. This comparative experiment is designed around the WRF and WRF-DA models as the central components. These models operate in a nested configuration, with the d01 having a horizontal resolution of 9 km and the d02 featuring a finer horizontal resolution of 3 km. The forecast area's geographical extent is illustrated in Figure 2, where the blue-filled area is the experimentally selected evaluation area in which the data will be used for performance comparisons with MCSPF-Net's precipitation forecasting results. The model is capable of generating high-resolution forecasts from 0 to 24 h and cyclically assimilating the forecasts on a 6-hourly cycle with daily start times of 00, 06, 12 and 18 h. The EC forecast data were used for the initial field and boundary conditions for the cold start and the boundary conditions for the hot start.

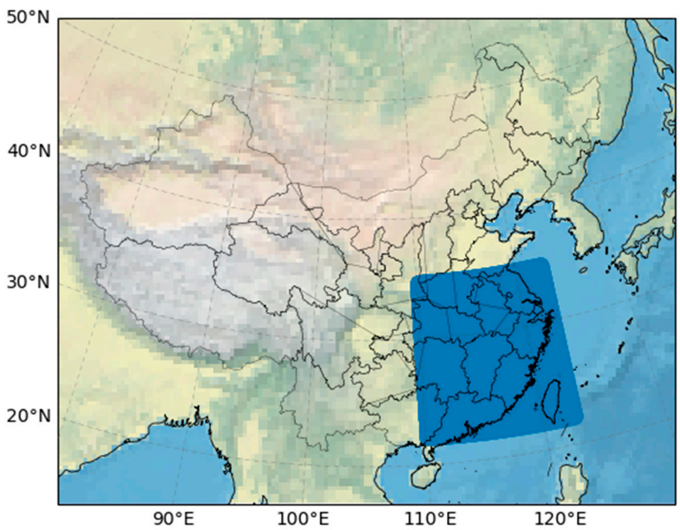

Figure 2. The forecast area's geographical extent and the experimentally selected evaluation area.

The PERSIANN-CCS product was used as an ANN-based quantitative precipitation estimate in the evaluation of the results. The PERSIANN-CCS has a time-resolution of 1 h and a spatial resolution of 0.04° × 0.04°. Precipitation estimation products covering the range of 60°S to 60°N provide usable quantitative precipitation estimation products for most parts of the world. The PERSIANN-CCS is distributed by the Center for Hydrometeorology and Remote Sensing (CHRS) at the University of California, Irvine (UCI). The PERSIANN-CCS product is available online: https://chrsdata.eng.uci.edu/ (accessed on 9 September 2023).

2.3. Data Pre-Processing

In this study, the experimental area was set as the southeast coastal area of China, with a latitude and longitude range of 22–34.75°N, 110–122.75°E, and a spatial resolution of 0.05° × 0.05°. Firstly, the observation data of AGRI water vapor and infrared band of the FY-4A satellite are calibrated and projected according to the brightness temperature, and the row and column numbers contained in the data are converted into latitude and longitude. The converted observation data of FY-4A are cut to the experimental area according to latitude and longitude. The quality control of the data after data pre-processing is carried out to prevent the missing data from affecting the model training process. Similarly, GPM-IMERG was pruned according to the experimental area selected in this study. The spatial resolution of GPM-IMERG data is 0.1° × 0.1° in order to match GPM-IMERG with FY-4A observation data in space. Therefore, GPM-IMERG needs to be interpolated to a spatial resolution of 0.05° × 0.05°, and the interpolation method is linear interpolation. Finally, the time matching of the two data is performed with a time interval of 30 min.

The data pre-processing process is shown in Figure 3a, and the data after time matching and stacking are shown in Figure 3b,c. The construction diagram of the input data is shown in Figure 3b. The AGRI multi-band brightness temperature observation data and the brightness temperature difference are stacked to obtain the AGRI observation matrix at one moment. The data dimension is channel × 256 × 256, where the channel will change with the combination of different bands. The stacked data need to be judged for time continuity. When the time of eight consecutive frames (240 min) is continuous, these data will be combined into time series data with a data dimension of channel × 8 × 256 × 256. In other words, it is assumed that the current real-time observation time is T time, and the input data time is T-210 min to T time. Figure 3c shows the construction diagram of the label data. The GPM-IMERG data also need to be judged for time continuity. When the data are continuous between T + 30 min and T + 240 min, the data will be combined into 1 × 8 × 256 × 256 dimensions. The two parts of data together form a multi-channel satellite precipitation forecasting dataset, which is used for model training and testing.

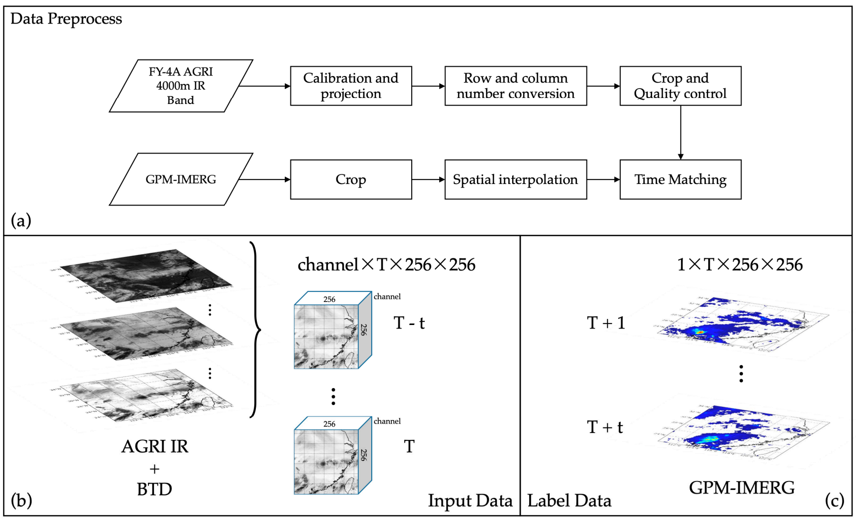

Figure 3. The data pre-processing process. (**a**) data preprocess (**b**) input data (**c**) label data.

3. Method

In this section, the multi-channel satellite short-term precipitation forecasting model proposed in this study will be introduced. The network structure, network training methods and evaluation methods of precipitation forecasting results will be introduced, respectively.

3.1. MCSPF-Net

This study proposes a multi-channel satellite precipitation forecasting method based on three-dimensional convolution. Three-dimensional convolution has been widely proven to have a learning ability for changes in temporal features [42]. This study takes into account the observed characteristics of the FY-4A satellite AGRI, and it requires the network to be able to simultaneously process the information in the multi-channel satellite observation images and capture the spatial and temporal variation characteristics of precipitation. Based on this feature, three-dimensional convolution is used to learn the temporal variation characteristics of satellite images and to learn the correlation between infrared band information and precipitation in multi-channel observation images. The precipitation forecasting based on multi-channel satellite observation images are realized.

The combination of input and output data of the network is shown in Figure 4a,b. Since the model training process uses a mini-batch size training scheme, a new batch dimension needs to be added for each preprocessed input and labeled data. After adjustment, the dimension of input data becomes batch $\times$ channel $\times$ 8 $\times$ 256 $\times$ 256 and the dimension of labeled data becomes batch $\times$ 1 $\times$ 8 $\times$ 256 $\times$ 256. In the process of network design, the U-Net structure is used as the basic structure of the network [43]. The network uses four down-sampling and four up-sampling structures to compress and restore multi-channel satellite observation images. In this process, the quantitative relationship between satellite multi-channel observation information and precipitation is learned, and finally, the minute-level satellite precipitation forecasting results are obtained. During each down-sampling process, the spatial and temporal scales of the data will be encoded, and the channel dimension information will be expanded. In this process, the network will learn the correlation between multi-channel observation images and precipitation [44]. At the same time, as the data are continuously compressed, the relative network will obtain an expanding spatial receptive field and improve the model's ability to estimate motion. In the up-sampling process, the data will be continuously restored in stages. Thanks to the existence of long jump connections, the valuable original information is well preserved in this process. The restored information outputs multi-period satellite precipitation forecasting results through a separate output layer. The network structure of MCSPF-Net is shown in Figure 4c.

Precipitation is a complex atmospheric process. In order to enhance the network and capture the temporal and spatial variation characteristics of different scales, this paper uses the idea of inception to design a multi-scale feature extraction module. The structure of the multi-scale feature extraction module is shown in Figure 4e. In this module, the input data will be copied into 4 copies, and the 3D convolutional layers with the kernel size of 1, 3, 5, and 7 will be used to extract the feature information of different scales. At the same time, the convolutional layers adopt the idea of depthwise separable convolution [31,32], and the 3D convolutional layers are split into the structure shown in the figure, which will significantly reduce the number of model parameters while ensuring the feature extraction capability of the model. The outputs of the different parts are concatenated and fed into a 1 $\times$ 1 $\times$ 1 convolutional layer, adjusting the channel dimensionality of the output information. Each convolutional layer uses GELU as the activation function, and a batch normalization is added at the end of the module to normalize the data. In order to reduce the information loss in the multi-scale feature extraction module, a residual connection is introduced in the module, and the data extracted by the module feature will be added to the original data to obtain a new result, reducing the information loss caused by the module feature extraction. In addition, the double convolution layer based on the Res-Net is added to the shallow layer of the network of MCSPF-Net for enhancing the precipitation forecasting speed of the model [45], and the structure of the double convolution layer is shown in Figure 4d.

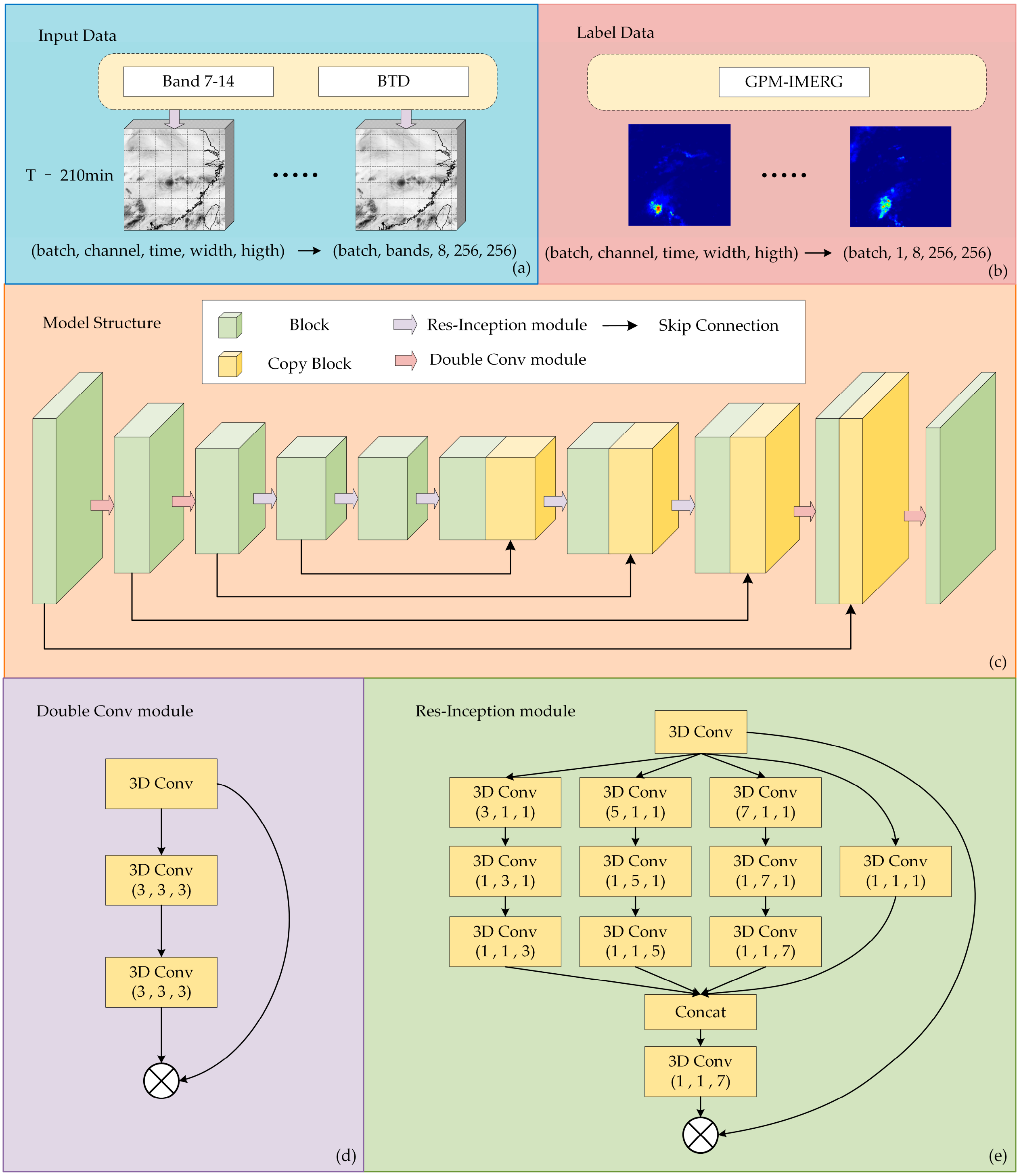

Figure 4. Detailed structure of models for (**a**) input data construction method, (**b**) label data construction method, (**c**) multi-channel satellite precipitation forecasting network, (**d**) double convolution layer, and (**e**) multi-scale feature extraction module.

3.2. Training Methods

The training and test datasets of this study used multi-channel observed images from FY-4A AGRI and GPM-IMERG products, and the scheme presented in Section 2.3 was used for dataset construction. The time of the dataset was chosen as April–October 2018–2020. Due to the climatic characteristics of China, precipitation occurs more frequently in the April–October period, so the choice of such a time point helps to better evaluate the model's ability to forecast precipitation. The datasets constructed from the two types of data need to be divided before the network training starts with 28,700 time series as the training dataset of the network and 6396 time series as the testing dataset of the network. The training dataset was entered into the model training using a random input scheme, while the testing dataset used a sequential input scheme. Due to the complexity of the precipitation task, the loss function in the network training process was chosen as MSE + αL1 Loss. It was found experimentally that the forecasting performance of the network had a more balanced performance when α was taken as 1. Adam was used as the optimizer in the network training process [46], and the early-stopping training strategy was also adopted. A dynamic learning rate setting was used for the network training process, and One-Cycle was adopted as the adjustment scheme for the learning rate with the highest learning rate of 0.05. The variation of the learning rate with the number of iterations is shown in Figure 5. Our network was built by the Pytorch framework and trained on an NVIDIA RTX3090 graphics card.

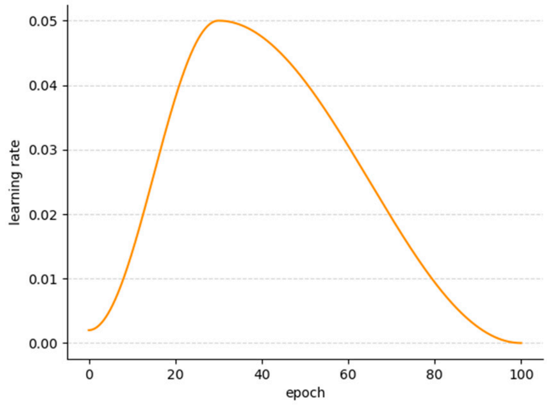

Figure 5. The variation of the learning rate with the number of iterations.

3.3. Experiment Design

Some precipitation inversion work based on GEO satellites has proved that more band information can bring better precipitation inversion results. Therefore, the experimental scheme will contain more abundant band information as much as possible. This study will compare different channel combination schemes, hoping to obtain the best channel combination scheme for satellite-based short-term precipitation forecasting and achieve the best forecasting performance. The combination scheme of the band mainly includes mid-wave infrared, water vapor, long-wave infrared, and bright temperature difference (BTD). Because the observation information between different observation bands has different emphases, it is necessary to judge which band observation information combination scheme can bring better forecasting performance to the satellite precipitation forecasting and which bands are redundant information for the results. Therefore, we combine the bands with different characteristics to test the influence of these band combinations on the precipitation task. Since the water vapor band has been widely proven to be of great significance to precipitation information, the water vapor band information is included in all combination schemes. In addition, the effects of the mid-wave infrared channel and BTD on precipitation forecasting were evaluated. By designing these band combination schemes, we were able to find the most suitable band combination scheme for precipitation forecasting. The spectral types, bands, and number of channels included in the band combination schemes used in this study are shown in Table 2.

Table 2. Band combination schemes.

No.	Spectrum Type	Waveband	Channel Number
1	Mid-wave infrared + Water vapor + Long-wave infrared + BTD	$IR_{3.75}$, $WV_{6.5}$, $WV_{7.2}$, $IR_{8.5}$, $IR_{10.7}$, $IR_{12.0}$, $IR_{13.3}$, $\Delta T_{10.7–6.25}$, $\Delta T_{10.7–13.3}$, $\Delta T_{12.0–7.2}$	11
2	Water vapor + Long-wave infrared + BTD	$WV_{6.5}$, $WV_{7.2}$, $IR_{8.5}$, $IR_{10.7}$, $IR_{12.0}$, $IR_{13.3}$, $\Delta T_{10.7–6.25}$, $\Delta T_{10.7–13.3}$	8
3	Water vapor + Long-wave infrared + BTD	$WV_{6.5}$, $WV_{7.2}$, $IR_{8.5}$, $IR_{10.7}$, $IR_{12.0}$, $IR_{13.3}$, $\Delta T_{10.7–6.25}$, $\Delta T_{10.7–13.3}$, $\Delta T_{12.0–7.2}$	9
4	Water vapor + Long-wave infrared + BTD	$WV_{6.5}$, $IR_{10.7}$, $IR_{13.3}$, $\Delta T_{10.7–6.25}$, $\Delta T_{10.7–13.3}$	5
5	Mid-wave infrared + Water vapor + Long-wave infrared	$IR_{3.75}$, $WV_{6.5}$, $WV_{7.2}$, $IR_{8.5}$, $IR_{10.7}$, $IR_{12.0}$, $IR_{13.3}$	8
6	Water vapor + Long-wave infrared	$WV_{6.5}$, $WV_{7.2}$, $IR_{8.5}$, $IR_{10.7}$, $IR_{12.0}$, $IR_{13.3}$	6

In the process of results evaluation, a variety of different evaluation metrics are used to assess the performance of MCSPF-Net in short-term precipitation forecasting. Among them, the quantitative evaluation metrics include mean square error (MSE), mean absolute error (MAE), and correlation coefficients (CCs) [47]. These metrics will be used to evaluate the numerical deviations of the model in forecasting precipitation rates. The metric formulas are shown in Equations (1)–(3).

$$\mathrm{MSE} = \frac{1}{m}\sum_{m}^{i=1}(x_i - y_i)^2 \quad (1)$$

$$\mathrm{MAE} = \frac{1}{m}\sum_{m}^{i=1}|x_i - y_i|^2 \quad (2)$$

$$\mathrm{CC} = \frac{\sum_{m}^{i=1}\left(x_i - \bar{x}\right)\left(y_i - \bar{y}\right)}{\sqrt{\sum_{m}^{i=1}\left(x_i - \bar{x}\right)^2}\sqrt{\sum_{m}^{i=1}\left(y_i - \bar{y}\right)^2}} \quad (3)$$

The classification evaluation metrics include three indicators: hit rate (POD), false alarm rate (FAR), and critical success index (CSI) [48]. They are used to evaluate the spatial match between the model output precipitation forecasting results and the actual precipitation. The formulas for the evaluation metrics are shown in Equations (4)–(6).

$$\mathrm{POD} = \frac{H}{(H+M)} \quad (4)$$

$$\mathrm{FAR} = \frac{F}{(H+F)} \quad (5)$$

$$\mathrm{CSI} = \frac{H}{(H+F+M)} \quad (6)$$

4. Evaluation

In this section, we will conduct several evaluations of the multi-channel satellite precipitation forecasting model. Firstly, we will quantitatively evaluate the forecasting performance of different band combination schemes for precipitation. Secondly, we will evaluate the spatial error distribution of precipitation forecasting results obtained from MCSPF-Net. Finally, we will analyze the spatial errors by comparing the model forecasting with rain gauge data from ground stations.

4.1. Performance Comparison of Band Combination Schemes in Precipitation Forecasting

Due to the characteristics of AGRI multi-channel observation, the observation results of AGRI contain information on many different bands. In order to find the most suitable band combination scheme for short-term precipitation forecasting, we evaluate the forecasting performance of the multiple band combination schemes designed in Section 3.3. The evaluation results of the band combination schemes used in this paper are shown in Figure 5, where the horizontal coordinates show the variation of the different forecast lead times and the vertical coordinates show the variation of the precipitation forecasting performance indexes with time. The first row of images in Figure 6 represents three quantitative evaluation metrics, MSE, MAE, and CC, respectively, and the second row of images represents three qualitative evaluation metrics, POD, FAR, and CSI, respectively.

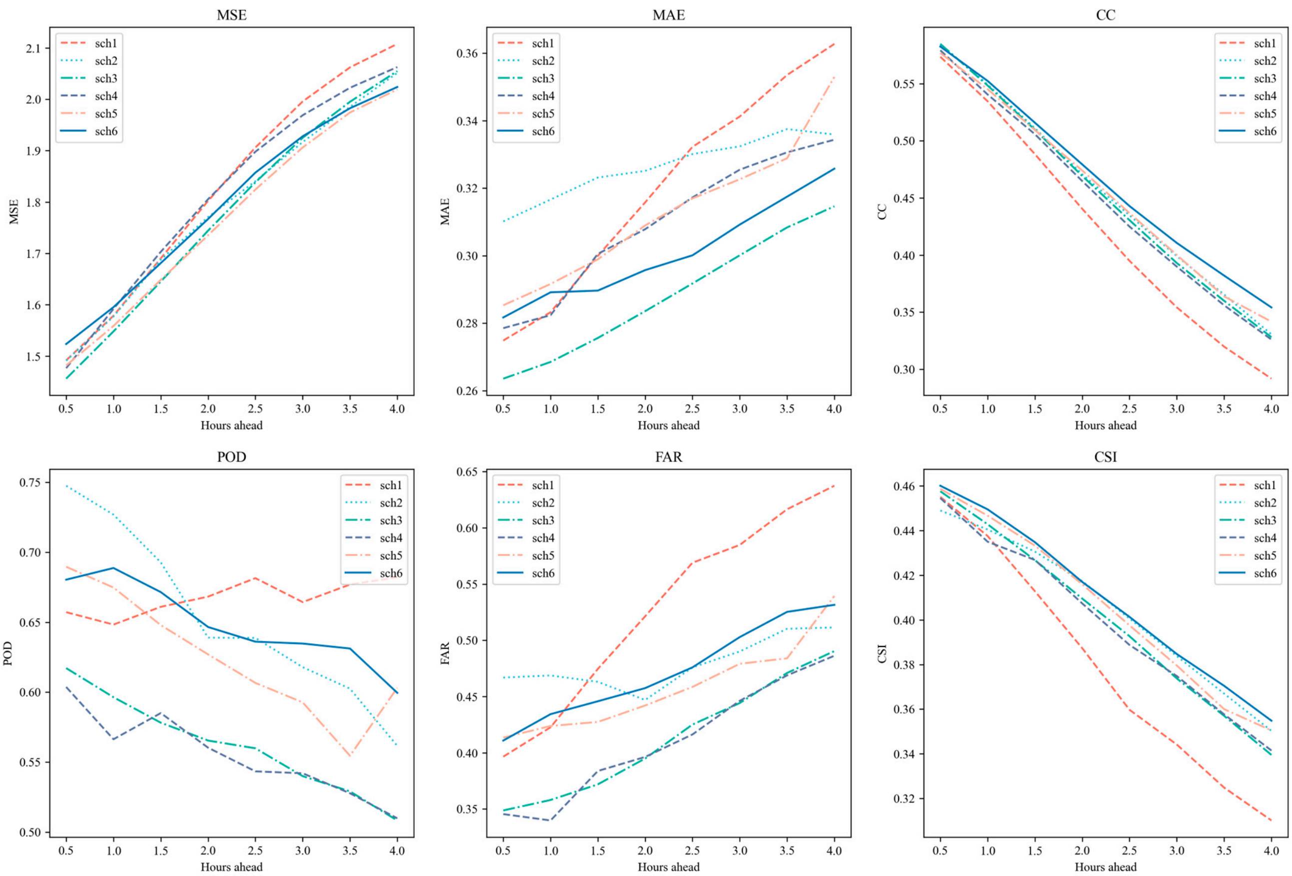

Figure 6. Quantitative evaluation results of band combination scheme with different forecast lead times.

In addition, the average results of the quantitative evaluation metrics for different band combination schemes were calculated to show the forecasting performance of different band combination schemes more clearly. The average quantitative evaluation results of the band combination scheme are shown in Table 3.

According to Table 3, MSE metrics and MAE metrics of several experimental schemes have different performances in the comparison. This discrepancy arises from the inherent nature of MSE, which amplifies larger errors and provides a more comprehensive evaluation of the presence of significant errors in precipitation forecasting results. On the other hand, MAE focuses on the overall level of errors and does not possess the magnification characteristic of MSE. Consequently, the divergence in the evaluation of MSE and MAE results in variations in the performance of multiple programs in terms of these metrics. Among the schemes evaluated, Scheme 1 includes all channels and the brightness temperature difference (BTD), providing a substantial amount of information. However, this abundance of information may lead to information redundancy, which ultimately affects the network forecasting performance. And bands 7,8 are affected by solar illumination due to their proximity to the visible and near-infrared bands, and the observation results are affected by solar illumination. The band combination schemes 1 and 5 are affected by diurnal variation, resulting in poor forecasting performance. The comparison of schemes 2, 3, and 6 reveals that the inclusion of the BTD leads to reduced errors in precipitation forecasting results. However, incorporating BTD has a negative impact on both the correlation coefficient and critical success index. This indicates that the BTD does not allow the model to better capture the precipitation trends when sufficient information is available. The comparison between schemes 2 and 4 indicates that the inclusion of a larger number of channels in the model leads to improved precipitation forecasting performance across multiple metrics. This suggests that the additional information provided by the additional channels has a positive effect on the model's ability to accurately forecast precipitation. In addition, we further statistically correlate the individual infrared bands and BTD with precipitation as a way to further explore the impact of different bands on precipitation forecasting. The calculated data will be displayed using correlation heat maps to show the distribution of correlations between individual bands and precipitation. The correlation heat map is shown in Figure 7, and the wavelength values are used to indicate the individual bands.

Table 3. Quantitative evaluation results of band combination scheme.

No.	POD	FAR	CSI	MSE	MAE	CC
1	0.667	0.528	0.379	1.829	0.320	0.425
2	0.653	0.479	0.405	1.790	0.326	0.456
3	0.562	0.413	0.400	1.776	0.288	0.453
4	0.555	0.410	0.398	1.816	0.310	0.448
5	0.625	0.458	0.405	1.769	0.313	0.456
6	0.649	0.473	0.409	1.795	0.301	0.465

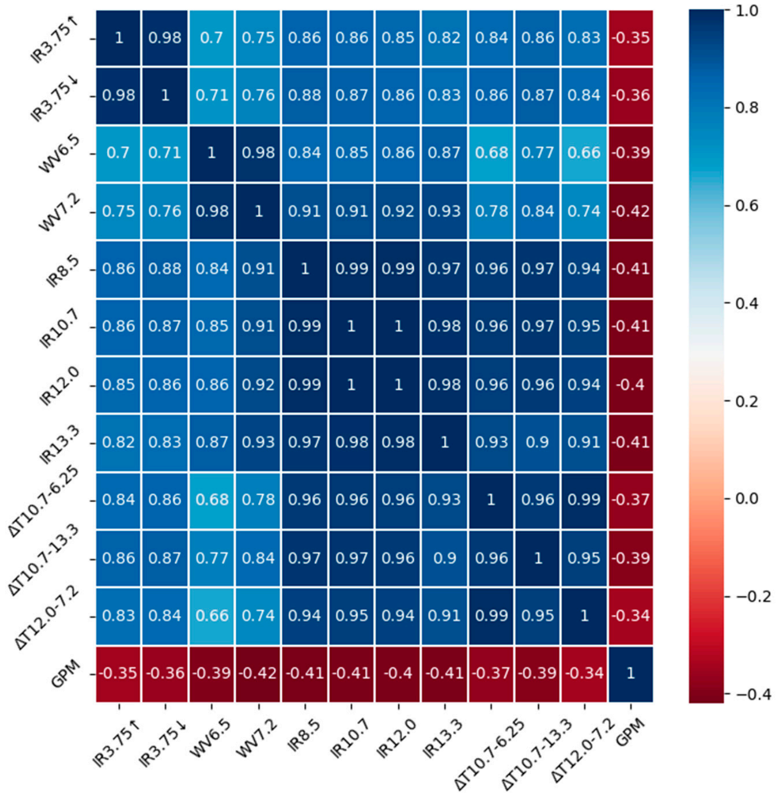

Figure 7. Heat map of correlation between all bands and precipitation.

The correlation of each band with precipitation according to Figure 7 also shows that the water vapor bands and the long-wave infrared bands show the higher correlation with precipitation. In contrast, the short-wave infrared bands and BTD have lower correlations with precipitation than the water vapor bands and the long-wave infrared bands. The results of the correlation heat map support the contribution of each band to the precipitation prediction in terms of numerical statistics, which also shows the high correlation between the band combination scheme used in scheme 6 and precipitation compared to the other schemes. Therefore, considering the balance of model forecasting performance on different metrics, band combination scheme 6 will be selected as the band combination scheme of the model in this study. In the subsequent evaluation, band combination scheme 6 will be selected and further evaluated for the precipitation forecasting results of the model, including spatial distribution analysis of precipitation errors and precipitation forecasting performance evaluation using rain gauges from ground-based observation sites.

4.2. Ablation Experiments

In this section, we conduct ablation experiments to validate the performance contribution of each module in the network for precipitation forecasting, which includes U-Net and Res-UNet using 3D convolution. In order to verify the effect of the number of Res-Inception modules and the number of layers on the precipitation prediction performance of the MCSPF-Net, we designed the MCSPF-Net network with different numbers of Res-Inception modules in the ablation experiments. In the ablation experiment, the position changes of the Res-Inception Module are shown in Figure 8. The figure shows where the different layers of the Res-Inception Module are added in the encoder part. The purpose of adding modules to deeper levels is to ensure that the Res-Inception module receives as much high-level semantic information as possible while reducing the risk of overfitting and minimizing the number of parameters. These experiments are used to quantitatively evaluate the impact of each module in MCSPF-Net on the performance of precipitation forecasting. The same quantitative evaluation metrics as in Section 4.1 were used in the ablation experiments, including POD, FAR, CSI, MSE, MAE, and CC. The average quantitative evaluation results of all the models in the ablation experiments are shown in Table 4. The layers marked behind the MCSPF-Net in Table 4 represent the number of the Res-Inception modules included in the model.

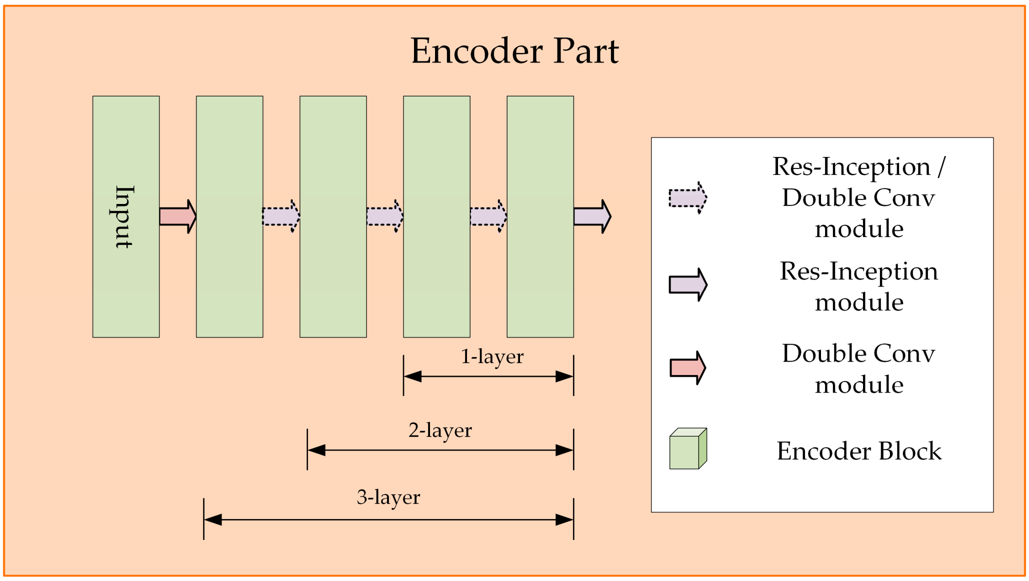

Figure 8. The position change of the Res-Inception Module in the ablation experiment.

Table 4. Quantitative evaluation results of all the models in ablation experiments.

Model	POD	FAR	CSI	MSE	MAE	CC
U-Net	0.790	0.572	0.386	1.804	0.330	0.457
Res-UNet	0.556	0.421	0.396	1.885	0.298	0.412
MCSPF-Net (1-layer)	0.617	0.449	0.408	1.860	0.300	0.434
MCSPF-Net (2-layer)	0.649	0.473	0.409	1.795	0.301	0.465
MCSPF-Net (3-layer)	0.564	0.435	0.390	1.799	0.293	0.453

The results of the comparisons in Table 4 show that MCSPF-Net achieves the best prediction performance in various key metrics (CSI, MSE, CC) with the 2-layer Res-Inception modules. While the 3-layer Res-Inception module did not further improve the prediction ability of the network, the network suffered from an overfitting problem during the training process, which affected the performance of the network in precipitation forecasting. For the network with the 1-layer Res-Inception module, the performance is worse than the network with the 2-layer Res-Inception modules. However, compared to Res-UNet, MCSPF-Net containing the 1-layer Res-Inception module achieves better performances in many metrics. Such performance shows that the Res-Inception module can help the network better capture the change pattern of precipitation, more accurately forecast the precipitation fallout area, and reduce the error. However, the number of Res-Inception modules is not enough to help the network bring better results, and it is necessary to reasonably configure the Res-Inception modules. Comparison results show that MCSPF-Net with 2-layer Res-Inception modules can achieve the best prediction performance. For U-Net integrating 3D convolution, due to the lack of residual connection in its structure, information loss occurs during the encoding process, which affects the feature extraction capability of the network. These reasons affect the precipitation forecasting performance of U-Net. Overall, adding the Res-Inception module to a suitable location in the network can enhance the precipitation forecasting ability of the network, obtaining more accurate precipitation fallout area and lower forecasting errors.

4.3. Spatial Distribution of Precipitation Forecasting Metric

The spatial distributions of the metrics over time for the precipitation forecasting results of MCSPF-Net are shown in Figure 9, using MAE, CSI and CC as the evaluated metrics, respectively. During the evaluation process, the spatial distribution statistics were conducted using the test dataset. The GPM-IMERG Final-Run product was chosen as the true value against which the model forecasting was compared. In Figure 9, the spatial distributions of MAE, CSI and CC for precipitation forecasting results are shown from left to right, and the variation of the metrics from 30 to 240 min of forecast lead times are shown from top to bottom, respectively.

According to the results in Figure 9, it can be seen that MAE tends to increase as the forecast lead time increases, indicating the accumulation of forecasting errors. The CSI and CC metrics tend to gradually decrease, indicating that the model's ability to forecast precipitation decreases after a longer period. These results are consistent with the characteristics of the deep learning network in short-term forecasting. The forecasting ability of the model will decrease gradually with the increase in forecast lead time. The spatial distribution of CSI and CC is more uniform, and the values of CC and CSI metrics decreases more smoothly with the increase in forecast lead time. This indicates that the network is better at precipitation forecasting areas. The precipitation forecasting results fit well with the GPM-IMERG product and can forecast future precipitation changes more accurately. Based on the variation of MAE, it can be found that there are regions in the middle and upper right of the image with larger MAE values, indicating higher forecasting errors in those regions. And the errors of precipitation forecasting are smaller in other regions. The error distribution characteristics have a large correlation with the precipitation characteristics of the region. To analyze this issue, further analysis was conducted.

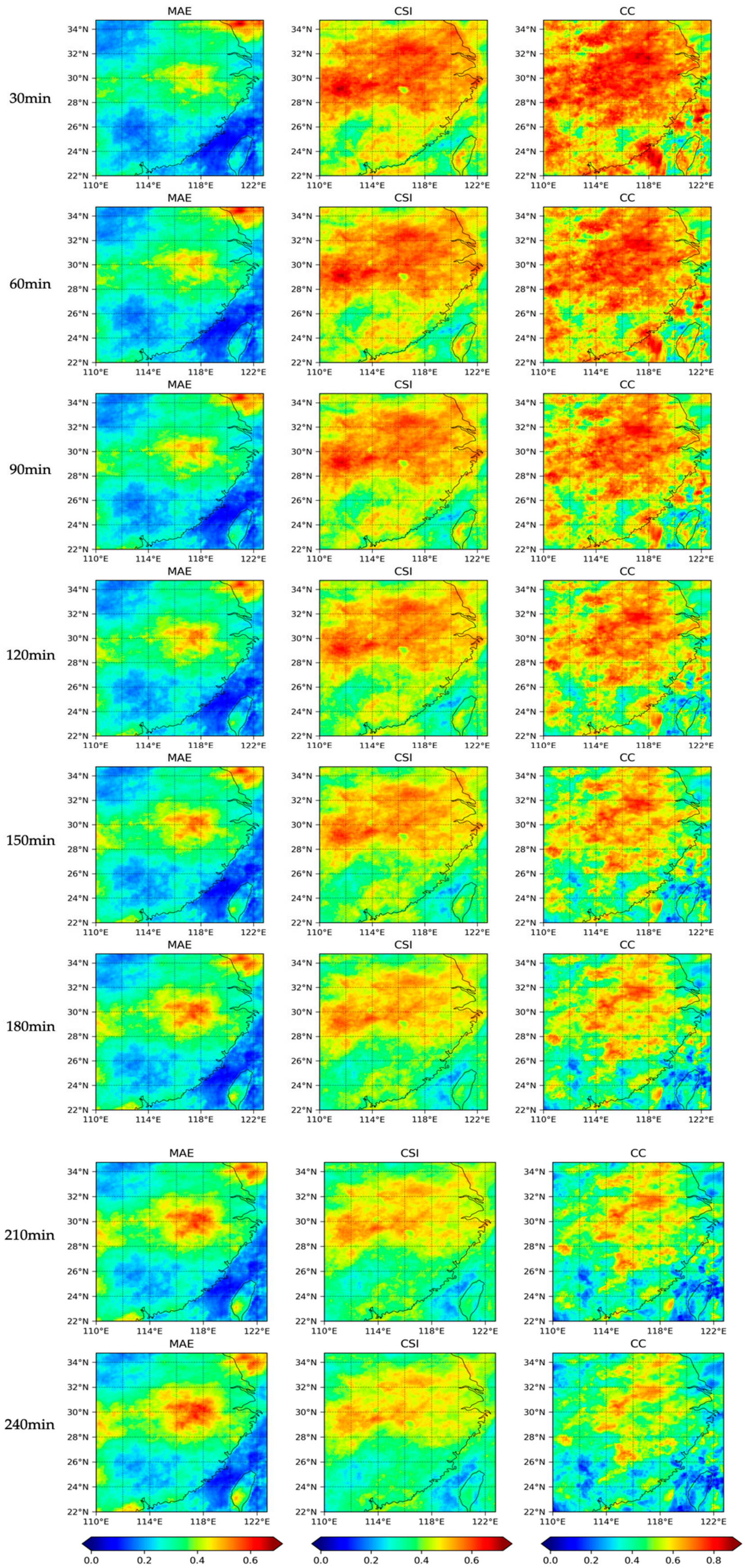

Figure 9. Spatial distribution of metrics forecasted in MCSPF-Net network for precipitation forecasting (example time May to September 2020).

In order to further analyze the characteristics of the distribution of spatial errors, we conducted statistics on the GPM-IMERG in the test dataset. The spatial distribution of the average precipitation and the spatial distribution of the precipitation frequency of the data in the test dataset were counted separately and used to analyze the causes of the spatial errors in Figure 9. According to the results in Figure 10, it can be found that the regions with larger MAE generally have larger average precipitation and lower precipitation frequency. This indicates that the single precipitation in the area is larger, which will lead to model errors bringing larger errors. Therefore, such a situation will be more significant in the value of MAE. In contrast, in the Taiwan Strait and its surrounding areas, where the precipitation is smaller and less frequent, the MAE index performs better. This also indicates that the network does not forecast well the extreme values of precipitation, resulting in high MAE indicators in some areas. In contrast, the performance of CSI and CC can be found to be better in areas with frequent or average precipitation, which also indicates the high accuracy of the network in forecasting the region of precipitation. For the same reason, the lower frequency of precipitation in the region around the Taiwan Strait leads to lower CSI and CC indicators in this region, and the forecasting performance decreases rapidly with the increasing forecast lead time compared to other regions. In general, MCSPF-Net can forecast the future 4 h precipitation changes better and can capture future precipitation trends better, but there is an underestimation problem for extreme precipitation.

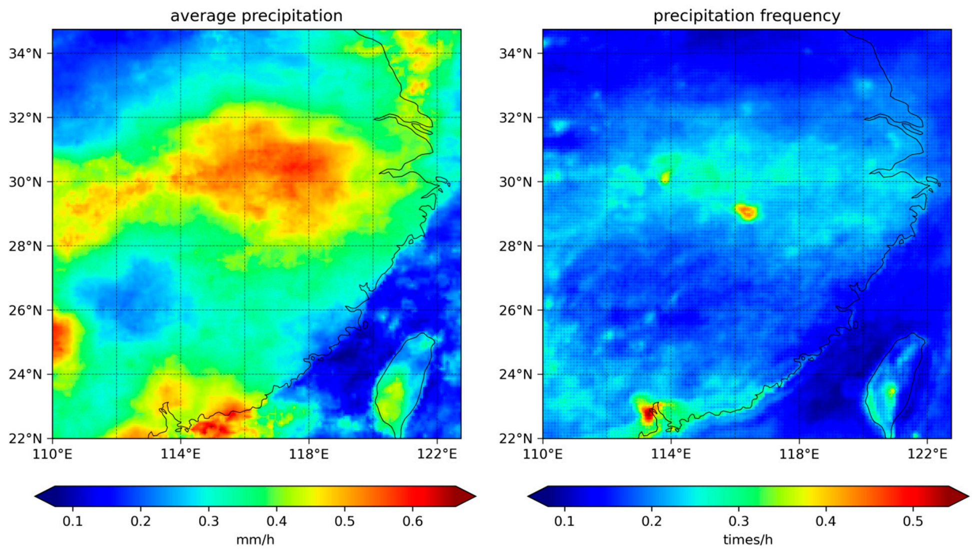

Figure 10. Regional average precipitation and precipitation frequency (example time May to September 2020).

4.4. Evaluation of Precipitation Forecasting Performance with Numerical Weather Prediction Model

In this section, the NWP model is introduced to evaluate the forecasting performance of precipitation models, and the ground-based rain gauge observations are introduced into the evaluation process for objectively evaluating the precipitation forecasting performance of the model. The data were used to assess the performance of precipitation forecasting using one-hour cumulative rainfall data from ground rain gauges in China, and MAE, CC and CSI metrics were selected as the evaluation metrics for precipitation forecasting results. The ground rain gauge data were used for the time-of-day assessment according to the forecast lead time of the precipitation forecast results.

We chose the forecast results of the last 4 h of each starting time of the d01 region as a comparison experiment and first clipped the forecast results of the d01 region to the region selected for the experiment. The forecast results of MCSPF-Net and WRF were evaluated hour by hour using rain gauges equipped at the ground stations, respectively. The results in Figure 11 show the spatial distribution of metrics for the precipitation forecasting results using ground rain gauge observations as true values. The first row of results in the figure represents the variation of MAE at different stations of MCSPF-Net during the 4 h forecast time and corresponds to the evaluation results of WRF below, which facilitates the comparison of the two performances. The six rows of images in Figure 11 represent the three metrics, MAE, CSI and CC, and a scatter plot is used to show the distribution of precipitation forecasting performance metrics.

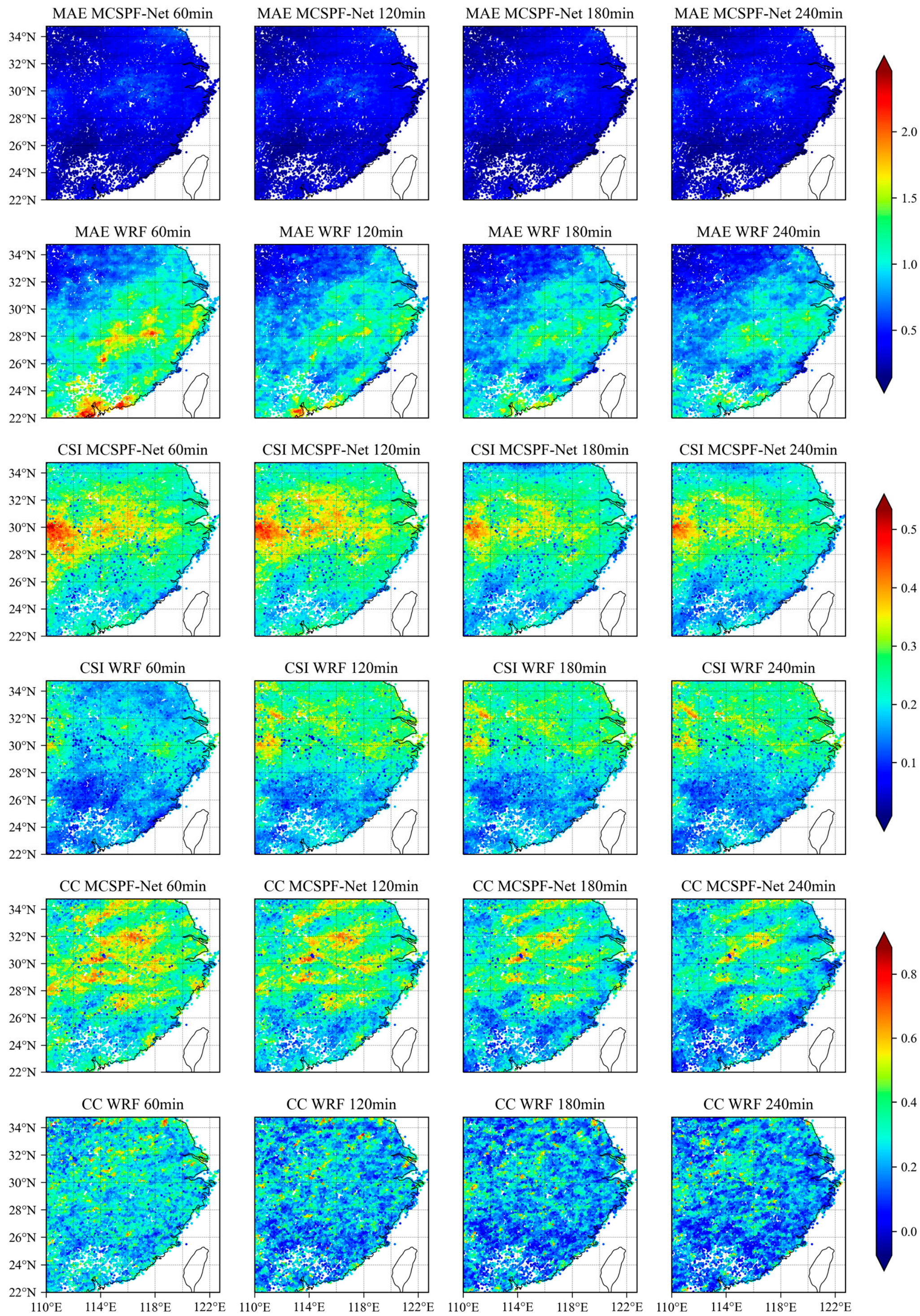

Figure 11. The spatial distribution of metrics for the precipitation forecasting results using ground rain gauge observations as true values (example time May to September 2020).

A comparison of precipitation forecasting results between MCSPF-Net and WRF is shown in Figure 11. According to Figure 11, the MAE of the MCSPF-Net network in the 4 h forecast experiment is significantly lower than that of WRF. For CSI and CC, the MCSPF-Net results obtain higher scores and more uniform distribution of the metrics. In addition, the WRF forecasts have a trend of increase and then decrease in the CSI metric. This indicates that the WRF is affected by the initial field accuracy in the short-term forecast. The evaluation results in Figure 11 illustrate that MCSPF-Net is able to better capture short-term precipitation patterns than WRF. Furthermore, MCSPF-Net exhibits a heightened accuracy in forecast future precipitation, obtaining a precipitation forecasts result that is closer to the actual situation. This attests to MCSPF-Net's advanced predictive prowess, particularly in its capacity to provide more precise and reliable short-term precipitation forecasts. Meanwhile, we calculated the average assessment metrics of the forecast results for MCSPF-Net and WRF at different forecast lead times, and the results are shown in Figure 12.

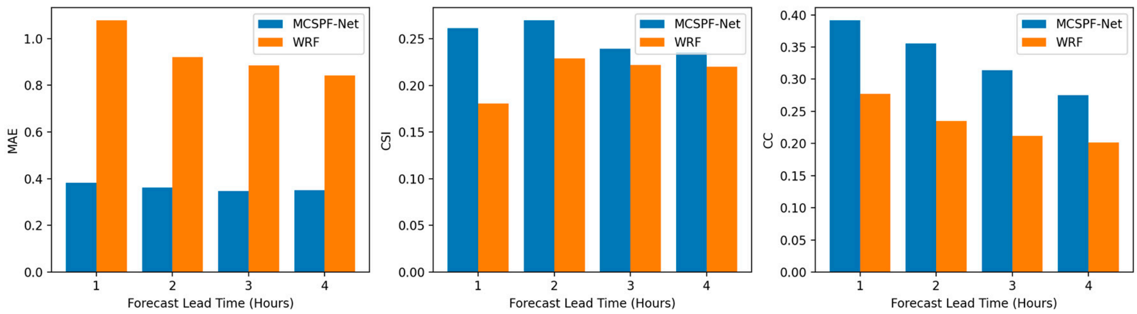

Figure 12. The average assessment metrics of the forecast results for MCSPF-Net and WRF at different forecast lead times (example time May to September 2020).

Figure 12 shows the quantitative evaluation result, illustrating the forecast performance of the two methods across varying forecast lead times. Based on the results in Figures 11 and 12, it can be found that WRF is continuously improving the performance of precipitation forecasting with increasing forecast lead time, the MAE is continuously decreasing, and the CSI is gradually increasing, decreasing the gap with MCSPF-Net. Regarding the CC metrics, it is noteworthy that while the correlation of the forecast results diminishes as the forecast lead time extends, WRF exhibits a gradual reduction in the disparity between itself and MCSPF-Net. For the NWP method, due to the spin-up problem, the model suffers from the incoherence of the dynamics, thermal and water cycle in the initial stage, and it takes some time to generate the correct cloud–water information, and this problem together with the accuracy of the initial field makes it difficult for the NWP method to generate accurate short-term precipitation forecasts. This is the reason for variations in the individual metrics of the NWP, and these trends also indicate some limitations of the NWP in short-term precipitation forecasting.

In addition, we have averaged the results of the ground rain gauge over time. The forecasting results of MCSPF-Net have better performance compared with the precipitation estimation products of PERSIANN-CCS, and the forecasting results of MCSPF-Net have lower MAE (0.36 vs. 0.37) performance with PERSIANN-CCS, higher CSI (0.25 vs. 0.17) and higher CC (0.33 vs. 0.20). Figure 13 shows the results of the spatial error distribution derived from the results of PERSIANN-CCS compared with the ground-based rain gauges. Compared to the PERSIANN-CCS precipitation estimation product, the forecasting generated by the MCSPF-Net network exhibits higher CSI and CC indicators. This proves that the forecasting results are more closely aligned with the actual surface precipitation conditions. Furthermore, the two methods demonstrate similar MAE metrics, indicating that the forecasting results of MCSPF-Net do not generate significant bias compared to the precipitation estimation.

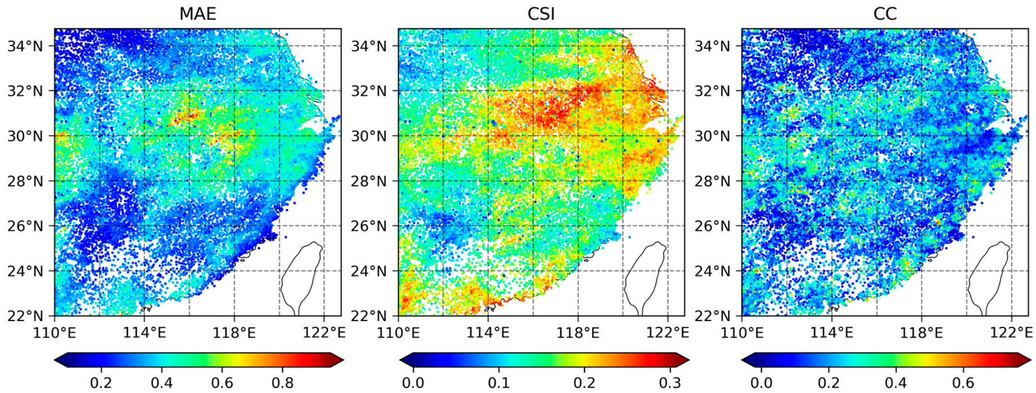

Figure 13. The spatial distribution of metrics for the PERSIANN-CCS results using ground rain gauge observations as true values (example time May to September 2020).

By comparing with both the NWP model and the PERSIANN-CCS, the precipitation forecast results of MCSPF-Net have better performance. This proves that MCSPF-Net has the capability to capture the numerical variation of precipitation effectively. Compared to precipitation estimation products based on deep learning networks, MCSPF-Net's forecasting results still have better performance. In general, the comparison results with ground rain gauges show that MCSPF-Net performs well in the task of short-term precipitation forecasting. It shows the ability to accurately forecast the spatial distribution of future precipitation and achieves a low forecasting error. This indicates that MCSPF-Net can effectively learn the variation characteristics of precipitation and can forecast precipitation more accurately.

5. Discussion

This study explores the feasibility of multi-channel infrared observation data of GEO meteorological satellites in short-term precipitation forecasting and quantitatively evaluates its performance. The results show that MCSPF-Net is able to forecast future precipitation variability well using multi-channel satellite observation images. Compared to NWP precipitation forecasting methods, MCSPF-Net generates precipitation forecasting results from real-time satellite observations, which are not affected by the initial field accuracy. Meanwhile, the 3D convolution deep learning network is trained to generate future forecast results in a few seconds, which greatly shortens the time required for forecast operation and reduces the amount of computation required for forecasting, which will increase the application scenarios of the network. Moreover, the fast operation speed of the deep learning network enables us to achieve short-term forecasts at the minute level effortlessly. This enhancement significantly improves the temporal and spatial resolution of the forecasting results, resulting in more refined and accurate forecasting outcomes. The continuous development and progress of meteorological satellites have led to a rapid improvement in the quality of satellite observation data. The method of precipitation estimation based on GEO satellites has demonstrated the effectiveness of using satellite observation data for accurate precipitation estimation. As satellite resolution and the availability of observation information continue to advance, satellite observation data will undoubtedly become a crucial source of observation data for precipitation forecasting in the future. This trend will contribute to more precise and reliable precipitation forecasts, benefiting various applications in weather prediction and climate studies.

However, there are still some limitations in the precipitation method based on GEO meteorological satellite infrared imaging. For one, the observation method based on GEO meteorological satellite infrared imaging with high spatial and temporal resolution can only obtain cloud top information, and it cannot obtain accurate three-dimensional structures of clouds. The precipitation estimation method based on the GEO meteorological satellite mainly depends on the relationship between the cloud top brightness temperature decrease and precipitation. However, precipitation estimation based on synchronous satellites is an indirect estimation method, and there are limitations in the precipitation estimation performance of GEO satellites compared to polar orbiting satellites equipped with microwave sensors. The precipitation estimation/forecasting products based on GEO meteorological satellites generally have the problem of low estimation results and misjudgment of precipitation area. Such problems limit the performance of GEO meteorological satellites in precipitation missions, which will become an important problem that GEO meteorological satellites need to solve in precipitation missions.

The current work proposed in this paper achieves more accurate short-term precipitation forecasting results, but there are still some limitations. Deep learning is a data-driven method by mining potential rules in a large number of historical samples. As a supervised learning method, the model relies on accurate precipitation products as labels. However, the labels available for precipitation forecasting at the current stage are still not perfect. For the GPM-IMERG product, its spatial resolution is $0.1^{\circ} \times 0.1^{\circ}$. Compared with the current mainstream GEO meteorological satellite, its product resolution is low, and it is easy to cause errors during interpolation. In addition, as a quantitative precipitation estimation product based on multi-satellite cooperative inversion, it still cannot accurately determine the actual precipitation area on the ground, which will also limit the forecasting accuracy of the precipitation forecasting model. In the future, we will try to introduce the observation data of polar orbiting satellites into the forecasting model to improve the performance of GEO meteorological satellites in precipitation forecasting. Furthermore, we will strive to acquire more precise precipitation data as ground-truth values for model forecasting. These efforts aim to further enhance the precipitation forecasting performance of the network.

6. Conclusions

This study proposes a multi-channel satellite precipitation forecasting model based on a 3D convolutional neural network. The MCSPF-Net utilizes multi-channel satellite observation sequence data as inputs to generate precipitation forecasting results for the upcoming four hours. This enables the network to achieve short-term precipitation forecasting with a high spatial and temporal resolution on a large scale. The results of the evaluation of multiple data sources show that the network can better forecast the spatial distribution of precipitation areas and capture the changes in precipitation. When compared to GPM-IMERG, the prediction results of our model have a high similarity, indicating that MCSPF-Net is able to learn the precipitation variation rule in GPM-IMERG. The average CSI of the forecasting results is 0.409, while the MSE is 1.795, the MAE is 0.301, and the CC is 0.465. When evaluated using rain gauges, the forecasting results of MCSPF-Net exhibited a higher critical success index (0.25 vs. 0.21) and correlation coefficients (0.33 vs. 0.23) and a lower mean square error (0.36 vs. 0.93) compared to the numerical weather prediction model. By comparing with both the NWP model and the PERSIANN-CCS, the precipitation forecast results of MCSPF-Net have better performance. This proved the efficacy of MCSPF-Net in precipitation forecasting patterns in the short term. Following extensive evaluation, this method has demonstrated its effectiveness in large-scale precipitation forecasting. This approach enables the short-term forecasting of precipitation over large areas by exploiting the extensive coverage and high-frequency observing capabilities of GEO satellites.

Author Contributions: Conceptualization, Y.J. and W.C.; methodology, Y.J. and W.C.; software, Y.J.; validation, Y.J., W.C. and F.G.; formal analysis, Y.J. and S.Z.; investigation, Y.J.; resources, F.G. and S.Z.; data curation, S.W. and C.L.; writing—original draft preparation, Y.J.; writing—review and editing, Y.J. and S.Z.; visualization, Y.J.; supervision, S.Z.; project administration, S.Z.; funding acquisition, C.L. and S.Z. All authors have read and agreed to the published version of the manuscript.

Funding: This work was supported by the Science and Technology Innovation Project of Laoshan Laboratory (LSKJ202202200, LSKJ202202202), the National Key R&D Program of China (2022YFE0106400), the National Natural Science Foundation of China (41830964), and Shandong "Taishan" Scientist Program (ts201712017), the Key R&D plan of Heilongjiang Province (2022ZX01A15), Qingdao Science and Technology Planning Park Cultivation Program Project (23-1-5-yqpy-11-qy).

Acknowledgments: The authors would like to thank the China National Satellite Meteorological Center, the National Aeronautics and Space Administration and the Center for Hydrometeorology and Remote Sensing (CHRS) at the University of California for their data provision.

Conflicts of Interest: The authors declare no conflict of interest.

References

1. Pan, X.; Lu, Y.; Zhao, K.; Huang, H.; Wang, M.; Chen, H. Improving Nowcasting of Convective Development by Incorporating Polarimetric Radar Variables into a Deep-Learning Model. *Geophys. Res. Lett.* **2021**, *48*, e2021GL095302. [CrossRef]
2. Pan, B.; Hsu, K.; AghaKouchak, A.; Sorooshian, S. Improving Precipitation Estimation Using Convolutional Neural Network. *Water Resour. Res.* **2019**, *55*, 2301–2321. [CrossRef]
3. Ma, Z.; Xu, J.; Ma, Y.; Zhu, S.; He, K.; Zhang, S.; Ma, W.; Xu, X. AERA5-Asia: A Long-Term Asian Precipitation Dataset (0.1°, 1-Hourly, 1951–2015, Asia) Anchoring the ERA5-Land under the Total Volume Control by APHRODITE. *Bull. Am. Meteorol. Soc.* **2022**, *103*, E1146–E1171. [CrossRef]
4. Han, L.; Liang, H.; Chen, H.; Zhang, W.; Ge, Y. Convective Precipitation Nowcasting Using U-Net Model. *IEEE Trans. Geosci. Remote Sens.* **2022**, *60*, 1–8. [CrossRef]
5. Mekonnen, K.; Melesse, A.M.; Woldesenbet, T.A. Spatial Evaluation of Satellite-Retrieved Extreme Rainfall Rates in the Upper Awash River Basin, Ethiopia. *Atmos. Res.* **2021**, *249*, 105297. [CrossRef]
6. Wei, C.-C.; Huang, T.-H. Modular Neural Networks with Fully Convolutional Networks for Typhoon-Induced Short-Term Rainfall Predictions. *Sensors* **2021**, *21*, 4200. [CrossRef]
7. Hwang, Y.; Clark, A.J.; Lakshmanan, V.; Koch, S.E. Improved Nowcasts by Blending Extrapolation and Model Forecasts. *Weather Forecast.* **2015**, *30*, 1201–1217. [CrossRef]
8. Shakti, P.C.; Misumi, R.; Nakatani, T.; Iwanami, K.; Maki, M.; Seed, A.W.; Hirano, K. Comparison of Rainfall Nowcasting Derived from the STEPS Model and JMA Precipitation Nowcasts. *Hydrol. Res. Lett.* **2015**, *9*, 54–60. [CrossRef]
9. Bauer, P.; Thorpe, A.; Brunet, G. The Quiet Revolution of Numerical Weather Prediction. *Nature* **2015**, *525*, 47–55. [CrossRef]
10. Franch, G.; Maggio, V.; Coviello, L.; Pendesini, M.; Jurman, G.; Furlanello, C. TAASRAD19, a High-Resolution Weather Radar Reflectivity Dataset for Precipitation Nowcasting. *Sci. Data* **2020**, *7*, 234. [CrossRef]
11. Tran, Q.K.; Song, S.K. Song Multi-ChannelWeather Radar Echo Extrapolation with Convolutional Recurrent Neural Networks. *Remote Sens.* **2019**, *11*, 2303. [CrossRef]
12. Shi, X.; Chen, Z.; Wang, H.; Yeung, D.-Y.; Wong, W.; Woo, W. Convolutional LSTM Network: A Machine Learning Approach for Precipitation Nowcasting. In Proceedings of the 28th International Conference on Neural Information Processing Systems—Volume 1, Cambridge, MA, USA, 7–12 December 2015; MIT Press: Cambridge, MA, USA, 2015; pp. 802–810.
13. Wang, Y.; Wu, H.; Zhang, J.; Gao, Z.; Wang, J.; Yu, P.S.; Long, M. PredRNN: A Recurrent Neural Network for Spatiotemporal Predictive Learning. *IEEE Trans. Pattern Anal. Mach. Intell.* **2022**, *45*, 2208–2225. [CrossRef] [PubMed]
14. Sønderby, C.K.; Espeholt, L.; Heek, J.; Dehghani, M.; Oliver, A.; Salimans, T.; Agrawal, S.; Hickey, J.; Kalchbrenner, N. MetNet: A Neural Weather Model for Precipitation Forecasting. *arXiv* **2020**, arXiv:2003.12140.
15. Xue, M.; Hang, R.; Liu, Q.; Yuan, X.-T.; Lu, X. CNN-Based near-Real-Time Precipitation Estimation from Fengyun-2 Satellite over Xinjiang, China. *Atmos. Res.* **2021**, *250*, 105337. [CrossRef]
16. Hong, J.; Mao, F.; Gong, W.; Gan, Y.; Zang, L.; Quan, J.; Chen, J. Assimilating Fengyun-4A Observations to Improve WRF-Chem PM2.5 Predictions in China. *Atmos. Res.* **2022**, *265*, 105878. [CrossRef]
17. Ma, Z.; Zhu, S.; Yang, J. FY4QPE-MSA: An All-Day Near-Real-Time Quantitative Precipitation Estimation Framework Based on Multispectral Analysis from AGRI Onboard Chinese FY-4 Series Satellites. *IEEE Trans. Geosci. Remote Sens.* **2022**, *60*, 1–15. [CrossRef]
18. Yu, C.; Hu, D.; Liu, M.; Wang, S.; Di, Y. Spatio-Temporal Accuracy Evaluation of Three High-Resolution Satellite Precipitation Products in China Area. *Atmos. Res.* **2020**, *241*, 104952. [CrossRef]
19. Gao, Y.; Guan, J.; Zhang, F.; Wang, X.; Long, Z. Attention-Unet-Based Near-Real-Time Precipitation Estimation from Fengyun-4A Satellite Imageries. *Remote Sens.* **2022**, *14*, 2925. [CrossRef]
20. Zhao, H.; Yang, B.; Yang, S.; Huang, Y.; Dong, G.; Bai, J.; Wang, Z. Systematical Estimation of GPM-Based Global Satellite Mapping of Precipitation Products over China. *Atmos. Res.* **2018**, *201*, 206–217. [CrossRef]
21. Gebremicael, T.G. Satellite-Based Rainfall Estimates Evaluation Using a Parsimonious Hydrological Model in the Complex Climate and Topography of the Nile River Catchments. *Atmos. Res.* **2022**, *12*, 105939. [CrossRef]
22. Moazami, S.; Najafi, M.R. A Comprehensive Evaluation of GPM-IMERG V06 and MRMS with Hourly Ground-Based Precipitation Observations across Canada. *J. Hydrol.* **2021**, *594*, 125929. [CrossRef]
23. Sadeghi, M.; Asanjan, A.A.; Faridzad, M.; Nguyen, P.; Hsu, K.; Sorooshian, S.; Braithwaite, D. PERSIANN-CNN: Precipitation Estimation from Remotely Sensed Information Using Artificial Neural Networks–Convolutional Neural Networks. *J. Hydrometeorol.* **2019**, *20*, 2273–2289. [CrossRef]
24. Kim, T.; Yang, T.; Zhang, L.; Hong, Y. Near Real-Time Hurricane Rainfall Forecasting Using Convolutional Neural Network Models with Integrated Multi-SatellitE Retrievals for GPM (IMERG) Product. *Atmos. Res.* **2022**, *270*, 106037. [CrossRef]

25. Hayatbini, N.; Kong, B.; Hsu, K.; Nguyen, P.; Sorooshian, S.; Stephens, G.; Fowlkes, C.; Nemani, R. Conditional Generative Adversarial Networks (CGANs) for Near Real-Time Precipitation Estimation from Multispectral GOES-16 Satellite Imageries—PERSIANN-CGAN. *Remote Sens.* **2019**, *11*, 2193. [CrossRef]
26. Hsu, K.; Gao, X.; Sorooshian, S.; Gupta, H.V. Precipitation Estimation from Remotely Sensed Information Using Artificial Neural Networks. *J. Appl. Meteorol.* **1997**, *36*, 1176–1190. [CrossRef]
27. Hong, Y.; Hsu, K.-L.; Sorooshian, S.; Gao, X. Precipitation Estimation from Remotely Sensed Imagery Using an Artificial Neural Network Cloud Classification System. *J. Appl. Meteorol.* **2004**, *43*, 1834–1853. [CrossRef]
28. Wang, C.; Tang, G.; Xiong, W.; Ma, Z.; Zhu, S. Infrared Precipitation Estimation Using Convolutional Neural Network for FengYun Satellites. *J. Hydrol.* **2021**, *603*, 127113. [CrossRef]
29. Wang, C.; Xu, J.; Tang, G.; Yang, Y.; Hong, Y. Infrared Precipitation Estimation Using Convolutional Neural Network. *IEEE Trans. Geosci. Remote Sens.* **2020**, *58*, 8612–8625. [CrossRef]
30. Zhu, S.; Ma, Z. PECA-FY4A: Precipitation Estimation Using Chromatographic Analysis Methodology for Full-Disc Multispectral Observations from FengYun-4A/AGRI. *Remote Sens. Environ.* **2022**, *282*, 113234. [CrossRef]
31. Szegedy, C.; Vanhoucke, V.; Ioffe, S.; Shlens, J.; Wojna, Z. Rethinking the Inception Architecture for Computer Vision. *arXiv* **2015**, arXiv:1512.00567v3.
32. Xie, S.; Girshick, R.; Dollár, P.; Tu, Z.; He, K. Aggregated Residual Transformations for Deep Neural Networks. *arXiv* **2017**, arXiv:1611.05431.
33. Yang, J.; Zhang, Z.; Wei, C.; Lu, F.; Guo, Q. Introducing the New Generation of Chinese Geostationary Weather Satellites, Fengyun-4. *Bull. Am. Meteorol. Soc.* **2017**, *98*, 1637–1658. [CrossRef]
34. Xian, D.; Zhang, P.; Gao, L.; Sun, R.; Zhang, H.; Jia, X. Fengyun Meteorological Satellite Products for Earth System Science Applications. *Adv. Atmos. Sci.* **2021**, *38*, 1267–1284. [CrossRef]
35. Hu, Y.; Zhang, Y.; Yan, L.; Li, X.-M.; Dou, C.; Jia, G.; Si, Y.; Zhang, L. Evaluation of the Radiometric Calibration of FY4A-AGRI Thermal Infrared Data Using Lake Qinghai. *IEEE Trans. Geosci. Remote Sens.* **2021**, *59*, 8040–8050. [CrossRef]
36. Zhang, P.; Lu, Q.; Hu, X.; Gu, S.; Yang, L.; Min, M.; Chen, L.; Xu, N.; Sun, L.; Bai, W.; et al. Latest Progress of the Chinese Meteorological Satellite Program and Core Data Processing Technologies. *Adv. Atmos. Sci.* **2019**, *36*, 1027–1045. [CrossRef]
37. Zhang, A.; Xiao, L.; Min, C.; Chen, S.; Kulie, M.; Huang, C.; Liang, Z. Evaluation of Latest GPM-Era High-Resolution Satellite Precipitation Products during the May 2017 Guangdong Extreme Rainfall Event. *Atmos. Res.* **2019**, *216*, 76–85. [CrossRef]
38. Anjum, M.N.; Ding, Y.; Shangguan, D.; Ahmad, I.; Ijaz, M.W.; Farid, H.U.; Yagoub, Y.E.; Zaman, M.; Adnan, M. Performance Evaluation of Latest Integrated Multi-Satellite Retrievals for Global Precipitation Measurement (IMERG) over the Northern Highlands of Pakistan. *Atmos. Res.* **2018**, *205*, 134–146. [CrossRef]
39. Wang, Z.; Zhong, R.; Lai, C.; Chen, J. Evaluation of the GPM IMERG Satellite-Based Precipitation Products and the Hydrological Utility. *Atmos. Res.* **2017**, *196*, 151–163. [CrossRef]
40. Pradhan, R.K.; Markonis, Y.; Vargas Godoy, M.R.; Villalba-Pradas, A.; Andreadis, K.M.; Nikolopoulos, E.I.; Papalexiou, S.M.; Rahim, A.; Tapiador, F.J.; Hanel, M. Review of GPM IMERG Performance: A Global Perspective. *Remote Sens. Environ.* **2022**, *268*, 112754. [CrossRef]
41. Sungmin, O.; Foelsche, U.; Kirchengast, G.; Fuchsberger, J.; Tan, J.; Petersen, W.A. Evaluation of GPM IMERG Early, Late, and Final Rainfall Estimates Using WegenerNet Gauge Data in Southeastern Austria. *Hydrol. Earth Syst. Sci.* **2017**, *21*, 6559–6572. [CrossRef]
42. Zhou, K.; Zheng, Y.; Dong, W.; Wang, T. A Deep Learning Network for Cloud-to-Ground Lightning Nowcasting with Multisource Data. *J. Atmos. Ocean. Technol.* **2020**, *37*, 927–942. [CrossRef]
43. Ronneberger, O.; Fischer, P.; Brox, T. U-Net: Convolutional Networks for Biomedical Image Segmentation. In *Medical Image Computing and Computer-Assisted Intervention—MICCAI 2015*; Navab, N., Hornegger, J., Wells, W.M., Frangi, A.F., Eds.; Lecture Notes in Computer Science; Springer International Publishing: Cham, Switzerland, 2015; Volume 9351, pp. 234–241, ISBN 978-3-319-24573-7.
44. Noh, H.; Hong, S.; Han, B. Learning Deconvolution Network for Semantic Segmentation. In Proceedings of the 2015 IEEE International Conference on Computer Vision (ICCV), Santiago, Chile, 7–13 December 2015; IEEE: Santiago, Chile, 2015; pp. 1520–1528.
45. He, K.; Zhang, X.; Ren, S.; Sun, J. Deep Residual Learning for Image Recognition. In Proceedings of the 2016 IEEE Conference on Computer Vision and Pattern Recognition (CVPR), Las Vegas, NV, USA, 27–30 June 2016; IEEE: Las Vegas, NV, USA, 2016; pp. 770–778.
46. Kingma, D.P.; Ba, J. Adam: A method for stochastic optimization. *arXiv* **2014**, arXiv:1412.6980.
47. Yang, X.; Zhao, C.; Luo, N.; Zhao, W.; Shi, W.; Yan, X. Evaluation and Comparison of Himawari-8 L2 V1.0, V2.1 and MODIS C6.1 Aerosol Products over Asia and the Oceania Regions. *Atmos. Environ.* **2020**, *220*, 117068. [CrossRef]
48. Yang, Y.; Sun, W.; Chi, Y.; Yan, X.; Fan, H.; Yang, X.; Ma, Z.; Wang, Q.; Zhao, C. Machine Learning-Based Retrieval of Day and Night Cloud Macrophysical Parameters over East Asia Using Himawari-8 Data. *Remote Sens. Environ.* **2022**, *273*, 112971. [CrossRef]